ASE recirculation effects in pulsed frequency shifted feedback lasers at large frequency shifts

MIGUEL CUENCA[1], HAROLDO MAESTRE[1], GERMÁN TORREGROSA[1], HUGUES GUILLET DE CHATELLUS[2], AND CARLOS R. FERNÁNDEZ-POUSA[1,*]

[1]*Engineering Research Institute I3E, Univ. Miguel Hernández, Av. Universidad s/n, 03202 Elche, Spain*
[2]*Institut FOTON, Université de Rennes, 263 Av. Général Leclerc, 35042 Rennes, France*
[*]c.pousa@umh.es

Abstract: An analysis of the different emission regimes (continuous wave, Q-switched, and different forms of modelocking) of a C-band Er:fiber frequency shifted feedback laser at large frequency shifts is presented. We clarify the role of ASE recirculation in the origin of various spectral and dynamical properties of this type of lasers. Specifically, we show that Q-switched pulses are supported by a noisy, quasiperiodic ASE recirculation pattern that univocally identifies the pulses within the sequence, and that these Q-switched pulses are chirped as a consequence of the frequency shift. A specific pattern of ASE recirculation, in the form of a periodic stream of pulses, is identified in resonant cavities, namely, those where the free spectral range and the shifting frequency are commensurable. The phenomenology associated with this pattern is explained through the moving comb model of ASE recirculation. Modelocked emission is induced from both integer and fractional resonant conditions. It is shown that ASE recirculation coexists with modelocked pulses, originates a secondary peak in the optical spectrum, and also drives Q-switched modelocking near resonant conditions. Harmonic modelocking with variable harmonic index is also observed in non-resonant cavities.

1. Introduction

The incorporation of a frequency-shifting (FS) element in a laser cavity has been long known to produce an amplified output without the Fabry-Pérot (FP) mode structure of standard lasers [1, 2]. It is also known that these Frequency-Shifted Feedback (FSF) lasers are amenable to oscillation in different dynamical regimes, both continuous-wave (CW) and pulsed, and so they have been demonstrated in a variety of gain media, emission bands, and cavity configurations [3–19]. The simplicity of the FSF laser architecture has gained renewed attention for the generation of pulsed emissions in the mid infrared (MIR) band, where more conventional techniques may become difficult to implement [20–25]. In this band, a wide range of materials shows strong molecular absorption signatures and, thus, MIR laser emission finds applications in molecular spectroscopy, sensing, nonlinear optics, medical applications, and line-of-sight communications in the atmospheric transmission windows. Compact fiber sources based on doped fluoride and chalcogenide glasses represent an attractive and versatile alternative in this context [26, 27], and FSF lasers offers the possibility to generate pulsed emission by use of acousto-optics frequency shifters (AOFS) compatible with the wavelengths of interest.

Much of the current understanding on AOFS-driven FSF lasers relies on the studies following their first demonstrations [2–4]. The modeless emission of CW FSF lasers is understood as a consequence of the recirculation of ASE generated at the gain medium, the frequency shift f_s imparted in each roundtrip being responsible of the absence of frequency discrimination [2]. The buildup of pulsed emission, in turn, involves additional effects, specifically gain dynamics and Kerr-type nonlinear propagation [9]. A specific question is the role played in the laser

dynamics by the two scales involved in roundtrip propagation, namely the frequency shift f_s and the cavity's free spectral range FSR $= 1/\tau_c$, with τ_c the cavity's roundtrip time, in particular in the so-called resonant FS cavities [5–7]. A resonant cavity is defined by the condition that the product $f_s\tau_c$ has a fractional value; this product represents the phase gained after a roundtrip, in units of 2π, by a frequency-shifted wavelength. In the configuration of interest here –unseeded FSL lasers with intracavity bandwidth limiting filter– Sabert and Brinkmeyer [8, 9] identified the Q-switched (QS) and modelocked (ML) emission in Er and Yb:fiber FSF lasers in both linear and ring cavity configurations. They also showed the critical role of the spectral broadening induced by Kerr effect in the development of modelocking, as a means to compensate for the unidirectional spectral displacement induced by the frequency shifter and also to establish a phase distribution throughout the optical spectrum. In addition, they reported the buildup of harmonic modelocking (HML) with different harmonic indices in long fiber cavities and large pump powers. These results, which were obtained for small frequency shifts $f_s\tau_c < 1$, did not display any selectivity with respect to f_s.

Subsequent work [10, 11] implemented soliton fiber lasers in Er:fiber based on the related sliding-frequency filtering concept. Following [10], it was pointed out [12] that ML pulses need not dispersion to grow up in a FSF cavity, thus opening a different route for pulse buildup. QS, ML, and Q-switched ML (QML) regimes were also characterized by Perry et al. [13] at large, resonant frequency shifts $f_s\tau_c = 10$ in a linear-cavity Er:fiber FSF laser, and by Bonnet et al. [14, 15] in a linear-cavity Ti:sapphire FSF laser at nonresonant shifts $f_s\tau_c \lesssim 2$. The all-fiber ring-cavity Er:fiber configuration has also been studied by several authors, including the simulations studies of QS [16] and both experimentally and by numerical methods in the case of ML [17, 18]. The overall picture that arises from these accounts indicates that QS pulses are built as sustained relaxation oscillations [9], and show a time-varying optical spectrum induced by the frequency shift with accompanying small variations of the instantaneous gain [16]. ML and HML are induced by Kerr-type nonlinearity, and are in principle attainable at any frequency shift by use of a sufficiently large pump power [9]. Nonetheless, ML emission in resonant cavities shows specific features, such as distinctive pulse-like regimes [13] and lower requirements of pump power [20].

More recently, interesting dynamical and spectral aspects of pulsed FSF lasers, both in NIR and MIR bands, have been reported. The spectrum of QS and ML pulses is known to differ from CW [13, 14] and, in particular, ML emission with broad intracavity filters typically shows a double peak structure [17, 18, 21] that is not fully understood. At high pump levels, ML emission shows up in a multipulse regime [9, 17, 19–21] similar to passively ML fiber lasers [28]. Also, it has been identified a specific mechanism in the ML intensity spectrum that drives the QML dynamics [22], although its origin is unclear. Finally, a recent report has revealed the spectro-temporal structure of ML buildup at small frequency shifts [29].

The objective of this paper is to address the origin of these features and, in particular, show how the different forms of ASE recirculation are on the basis of these effects. Our approach is based on the systematic characterization of the pulsed regimes in a 1.55 μm Frequency-Shifting Loop (FSL). FSL are all-fiber systems targeted to high-bandwidth photonic signal processing and generation [30]. They are basically FSF lasers operated below threshold, and in its basic configuration they comprise a frequency shifting element, in our case an AOFS, an intra-loop amplifier, typically a low-noise EDFA, and a filter, all placed in a fiber ring configuration. FSF lasers and FSL, when these are operated above threshold, share the same underlying dynamics, and the versatility in the FSL implementation enables a precise control of the regimes where the loop progressively operates. Comparative information can then be extracted from standard spectral, radio-frequency (RF) and intensity characterization techniques, allowing for the isolation and identification of different dynamical features in each of the emission regimes.

With this approach we have explored the different pulsed regimes of FSL emission at integer,

fractional, and (approximately) irrational values of large products $f_s \tau_c$, a range that presents distinctive ASE recirculation patterns that constitute the starting point for our analysis. We describe here our main findings in parallel with the organization of the paper. After presenting our experimental system in Section 2 we introduce in Section 3 two standard models or recirculation in FS cavities, the so-called frequency-sliding filter model [6, 7, 31] and the moving comb (MC) model [7, 31–38]. This last model describes CW emission as a periodic stream of chirped waves and constitutes our theoretical basis for the interpretation of ASE recirculation. We then identify the observed dynamical regimes in terms of power and spectrum in Section 4 and in terms of EDFA dynamics in Section 5. In Section 6 we analyze two features of the QS regime that seem not to have been addressed in the literature: the intrinsic tagging of QS pulses provided by recirculating ASE and the demonstration of its chirped character, as predicted in the simulations of [16]. In Section 7 we analyze the ASE recirculation patterns that sustain CW and QS emission at large frequency shifts, identifying in both regimes a significant change at integer and fractional resonant conditions. At these values, ASE recirculates in periodic intensity patterns that resemble sequences of pulses with a periodicity equal to a harmonic of the shifting frequency. This pattern was identified at $f_s \tau_c = 10$ in [13] as a pulsed emission within the CW and QS regimes, but its origin as a particular form of ASE recirculation was not noticed. In Section 8, devoted to modelocking, we first induce ML for both integer and fractional values of $f_s \tau_c$. Emission appears as a cluster of pulses, or multipulse state [17, 21] together with a residual ASE recirculation field. Taking advantage of the particular form of ASE recirculation at resonant conditions, evidence is provided that the double peak in the ML spectra is associated to each of these two fields, ML pulses and ASE. We also show that this residual ASE field drives the ML dynamics near the resonance as was described in [22], in particular inducing QML. Away from resonant conditions, the emission evolves into a ML state composed of separated pulses that drift within the cavity's roundtrip time, state that can be stabilized either as QML or as HML, in this last case in a similar manner as was described in [9, 29] for small frequency shifts. Finally, we end in Section 9 with our conclusions.

Along with these findings we show that some of the observed features, specifically the phenomenology of the periodic intensity pattern of ASE recirculation, find a natural interpretation within the MC model. This observation is of relevance since it is known that at large frequency shifts $f_s \tau_c \geq 1$ the detection of recirculating chirps is not possible through direct spectral filtering [7, 32]. Thus, the present study not only shows the role played by ASE recirculation in various spectral and dynamical effects within the pulsed regimes of FSF lasers, but also supports the pertinence of the MC model of recirculation for large frequency shifts.

2. Experimental setup

As is shown in Fig. 1(a), the FSL is composed of an EDFA followed by a spectral filter and a fiber-coupled AOFS (AA Optoelectronic MT80-B10) providing positive frequency shifts around 80 MHz. An optical isolator is included before the EDFA to assure unidirectional circulation. The filter is an apodized uniform FBG (Technica T10) with a nominal central wavelength of 1550 nm, FWHM of 1.63 nm, peak reflectivity of 51%, and a reflectivity spectrum of approximately Gaussian shape, shown in Fig. 1(b). Polarization filter couplers were inserted before the AOFS and the isolator to extract the FSL output ($\simeq 2\%$ of the power at the EDFA output) and to inject a probe wavelength for the EDFA, respectively. In this last case, the probe wavelength is 1552.1 nm, near but out of the FBG reflection band, and is thus not subject to recirculation. This wavelength is extracted at the FBG transmission port after being spectrally filtered prior to detection by use of a tunable bandpass filter (EXFO XTM-50, not shown in the figure). The relative power variations of the probe wavelength provide a direct measurement of the single-pass EDFA gain.

In our default setting the cavity round-trip time τ_c, which was not actively stabilized, was 98.4 ns (loop length of ~19 m of fiber), although in specific experiments we varied the loop

length due to the experimental availability of some components. With these figures the accessible range of the product $f_s\tau_c$ is typically 7-8. Single-roundtrip losses were controlled through the RF power delivered to the AOFS and expressed in terms of the transmittance $T_{\text{pk}} < 1$ measured at 1550.0 nm, the wavelength that corresponds to the FBG reflectivity peak. Peak transmittance T_{pk} was calibrated in terms of the RF power driving the AOFS, up to a maximum value of -14.3 dB.
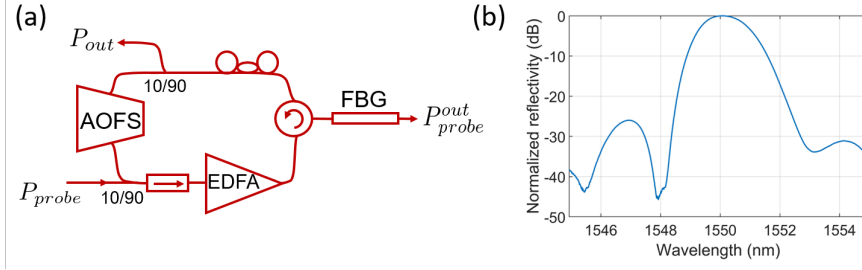

Fig. 1. (a) Experimental setup. (b) Normalized FBG reflectivity.

The EDFA was constructed from 60 cm of highly doped Erbium fiber (Liekki Er80/8) pumped at 978 nm with a power of ~160 mW, which amounts to ~10 times the doped fiber's transparency threshold. Amplifier's gain was fixed in our experiments, the loop's transparency being controlled through the AOFS driving power. Neither the amplifier nor the filter were built on polarization-maintaining fiber, so that a polarization controller was inserted before the output coupler to align the polarization. The EDFA showed a small-signal (unsaturated) gain $G_0 = 17.2$ dB, a saturation power $P_s = 12$ mW, and a noise figure <4.5 dB in the C band. In some occasions we induce a saturation in the EDFA through the probe wavelength, and denote as $G_{\text{ss}} \leq G_0$ the actual (small-signal) gain offered by the externally saturated EDFA when the ASE recirculation is small and hence does not contribute to an additional compression. This gain G_{ss} thus determines, under arbitrary compression conditions, the loop's threshold transparency $T_{\text{pk}}^{\text{th}}$ at the FBG reflectivity peak through the requirement that $G_{\text{ss}}T_{\text{pk}}^{\text{th}} = 1$.

3. Recirculation in a frequency-shifting cavity

3.1. The frequency-sliding filter

The frequency-sliding filter picture of light recirculation in a FS cavity is based on the evolution of monochromatic components in a passive cavity without frequency-selective filters [6,7]. In the case of a ring FS cavity it can presented as follows. We refer the intracavity field $\mathcal{E}(t)$ to the output of the AOFS, where the shift by f_s, here assumed positive, is imparted. The overall loop loss in amplitude is denoted by $\rho < 1$. Recirculation induces a recursive relationship between $\mathcal{E}(t)$ and its delayed, attenuated, and frequency-shifted replica of the form:

$$\mathcal{E}(t) = \rho e^{j2\pi f_s t}\mathcal{E}(t - \tau_c) + \mathcal{E}_{\text{in}}(t) \tag{1}$$

where we have assumed that propagation is linear and dispersionless and $\mathcal{E}_{\text{in}}(t)$ represents an injected input field. We note that in CW FSF lasers the seed field $\mathcal{E}_{\text{in}}(t)$ is the ASE produced by the amplifier, but (1) and therefore the present analysis is valid for any externally injected field.

Equation (1) defines a linear, time-variant system where $\mathcal{E}_{\text{in}}(t)$ is the input and $\mathcal{E}(t)$ the output. As can be checked by direct substitution, its solution is [7]:

$$\mathcal{E}(t) = \sum_{n=0}^{\infty} \rho^n e^{-j\pi f_s \tau_c n(n-1)} e^{j2\pi n f_s t}\mathcal{E}_{\text{in}}(t - n\tau_c) \tag{2}$$

On the other hand, the solution of a general linear, time-variant system can be expressed in terms of the Fourier spectrum $\widehat{\mathcal{E}}_{\text{in}}(\nu)$ of the input field in the general form [39]:

$$\mathcal{E}(t) = \int d\nu\, \widehat{\mathcal{E}}_{\text{in}}(\nu) T(\nu, t) e^{j2\pi\nu t} \tag{3}$$

where $T(\nu, t) e^{j2\pi\nu t}$ represents the time-spread response of the system to an oscillatory input $e^{j2\pi\nu t}$ of given frequency ν. Time-invariant systems are those for which $T(\nu, t)$ does not depend on t and so a monochromatic input only changes in amplitude and phase. Function $T(\nu, t)$ thus generalizes the concept of transfer function to time-variant systems. In the case at hand, it is given by a function of a single variable, $F(x)$ [7]:

$$T(\nu, t) = \sum_{n=0}^{\infty} \rho^n e^{-j\pi f_s \tau_c n(n-1)} e^{j2\pi n(f_s t - \nu \tau_c)} = F(\nu - \gamma_0 t) \tag{4}$$

where $\gamma_0 = f_s/\tau_c$ is the natural chirp rate of the FS cavity. Therefore, the system's frequency response at the initial instant $t = 0$, namely $T(\nu, 0) = F(\nu)$, slides in time according to rate γ_0. For rational values of the product $f_s \tau_c$, function $F(x)$ is known to be peaked at a series of equispaced passbands, a fact that is ultimately due to the temporal Talbot effect undergone by each of the recirculating optical frequencies [7]. Moreover, $F(x)$ reduces to an Airy function of equidistant Lorentzian lines in the limit of very small frequency shifts $f_s \tau_c \ll 1$ [7].

We mention that the present approach can be extended to CW FSF lasers by considering the recirculation of a monochromatic component in an active cavity with an intracavity bandwidth limiting filter. This leads to the so-called discrete frequency model [31]. In this case, the frequency response $T(\nu, t)$ of the associated linear system is no longer a frequency-sliding filter: the ρ^n factor in (4) transforms into a function $r_n(\nu)$ of the input frequency that accounts for the gain in amplitude accumulated by frequency ν after n recirculations. This results in a functional dependence of the form $T(\nu, t) = G(\nu - \gamma_0 t, \nu)$. The details can be consulted in Section 4 of [31].

3.2. The moving comb model

One of the consequences of the preceding frequency-sliding filter picture is that, when a chirped wave with chirp rate γ_0 is input in the FS cavity, the filter accompanies the wave, imparting on it a given amplitude and phase characteristics as in a linear, time-invariant filter. Starting from this observation we present the filtering properties of the FS cavity in a manner that highlights its similitude with a standard ring cavity, and apply it to the description of CW FSF laser emission. Let us decompose the output field $\mathcal{E}(t)$ in (1) in terms of waves chirped at γ_0, as shown is the left part of the following equation. The decomposition entails the spectrum of chirped waves, $C(\widetilde{\nu})$, which is defined in terms of $\mathcal{E}(t)$ by the inverse transform shown on the right part of the equation:

$$\mathcal{E}(t) = e^{j\pi f_s t^2/\tau_c} \int d\widetilde{\nu}\, C(\widetilde{\nu}) e^{j2\pi\widetilde{\nu} t} \qquad C(\widetilde{\nu}) = \int dt\, \mathcal{E}(t)\, e^{-j2\pi\widetilde{\nu} t - j\pi f_s t^2/\tau_c} \tag{5}$$

We also introduce the corresponding spectrum $C_{\text{in}}(\widetilde{\nu})$ that describes the input $\mathcal{E}_{\text{in}}(t)$. In this representation, the chirped waves have an instantaneous frequency $\nu_i(t) = \widetilde{\nu} + f_s t/\tau_c$, and so frequency $\widetilde{\nu}$ is not the standard optical (Fourier) component of a field, but its instantaneous frequency at a given reference time arbitrarily set to $t = 0$. Then, it is a simple task to show that the solution of (1) is given in $\widetilde{\nu}$ space in terms of the input field through an Airy transfer function $H_{\text{FS}}(\widetilde{\nu})$ similar to that of a FP filter, except for a shift in frequency by $f_s/2$:

$$C(\widetilde{\nu}) = H_{\text{FS}}(\widetilde{\nu})\, C_{\text{in}}(\widetilde{\nu}) = \frac{C_{\text{in}}(\widetilde{\nu})}{1 - \rho e^{-j2\pi(\widetilde{\nu} + f_s/2)\tau_c}} \tag{6}$$
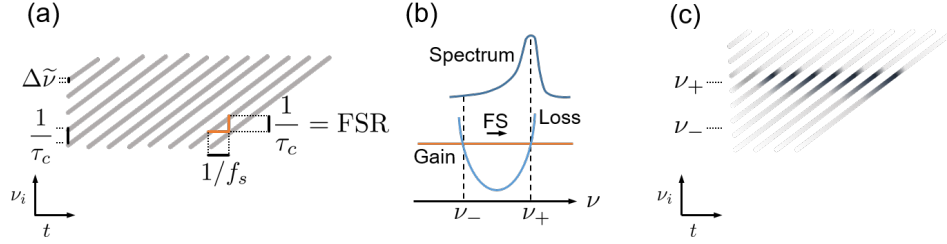
Fig. 2. (a) Schematics in the ν_i vs. t plane of the chirped fields in a linear dispersionless FS cavity without bandwidth limiting filter. (b) Net gain region in an active FS cavity with bandwidth limiting filter, and schematics of the resulting CW optical spectrum. (c) Schematics in the ν_i vs. t plane of the chirped fields in an active FS cavity with bandwidth limiting filter.

For $\rho \to 1$ the FS cavity thus selects frequencies $\widetilde{\nu}_k = \frac{k}{\tau_c} - \frac{f_s}{2}$ for integer k [35], in the form of sharp passbands of width $\Delta\widetilde{\nu} \ll 1/\tau_c$. The field is then described by a set of chirped waves:

$$\mathcal{E}(t) = \sum_k A_k(t)\, e^{j2\pi\widetilde{\nu}_k t + j\pi f_s t^2/\tau_c} \tag{7}$$

where the slowly varying complex amplitude $A_k(t)$ are given by:

$$A_k(t) = \frac{1}{1-\rho} \int_{-\Delta\widetilde{\nu}/2}^{\Delta\widetilde{\nu}/2} d\eta\, C_{\mathrm{in}}(\widetilde{\nu}_k + \eta) e^{j2\pi\eta t} \tag{8}$$

Note that transformation (5) and thus both the transfer function $H_{\mathrm{FS}}(\widetilde{\nu})$ and the representation (7) reduce to a standard FP filtering when $f_s \to 0$.

Referring to the ν_i vs. t plane in Fig. 2(a), field (7) is represented by a set of chirped waves which, at a given time, show instantaneous frequencies separated by the cavity's free spectral range FSR $= 1/\tau_c$ and, at a given instantaneous frequency, flow with period $1/f_s$. These chirps have been detected in the form of a sequence of pulses with periodicity $1/f_s$ after narrowband optical filtering [32, 33]. Detection thus requires an optical filter with spectral width $< 1/\tau_c$ and temporal resolution $< 1/f_s$, conditions that can be jointly fulfilled only at small frequency shifts $f_s\tau_c < 1$ [7, 32]. The emitted field (7) is usually referred to as a moving comb, i.e., an optical frequency comb with teeth spectrally separated by $1/\tau_c$ and globally chirped at the natural rate of the FS cavity.

On the other hand, an active cavity can be operated above threshold ($\rho > 1$) provided that we include an intracavity filter that controls the growth of the recirculating fields. As is schematically shown in Fig. 2(b), the intracavity filter defines a region of net gain for optical Fourier components $\nu_- < \nu < \nu_+$. Waves whose instantaneous frequency is above ν_- amplify while flowing through the filter up to ν_+, where they become below threshold and progressively attenuate. In our case, this transit is adiabatic since the frequency shift is much lower than the filter's width, and therefore the amplitudes $A_k(t)$ in (7) still change slowly with time. As a result, a stationary optical spectrum is built with a pronounced peak at ν_+ [35], as is depicted in the upper part of Fig. 2(b). In addition, if the input field is uniformly generated in the region of net gain, as is the case of the ASE seeding a CW FSF laser, the observed emission at ν_+ is dominated by those frequencies that were generated at ν_- [9], since in this case the accumulated gain is the highest. The population of the different chirps in (7) is not necessarily uniform: for pump powers leading to operation near threshold the authors of [32] found that the chirps had all the same amplitude, but for increasing pump some chirps were absent and the rest were organized in periodic groups as a consequence, presumably, of nonlinear interactions.

According to (6), the FS cavity acts as a FP filter in $\widetilde{\nu}$ space that selects the instantaneous frequency and bandwidth of the constituent chirps (7). The amplitude and phase of these chirps is determined by chirp spectrum $C_{in}(\widetilde{\nu})$, a spectrum that *depends on both the input field and on the cavity*: its definition in (5) represents the Fourier decomposition of the input field after a quadratic phase modulation that depends on γ_0. In this regard, the present description of the filtering properties of a FS cavity is complementary to the sliding filter picture: in this last case, (3) indicates that the frequency response $T(\nu, t) = F(\nu - \gamma_0 t)$ is time dependent, but the input to the filter is simply the Fourier spectrum $\widehat{\mathcal{E}}_{in}(\nu)$ of the input field. In the present approach, (6) shows that the frequency response $H_{FS}(\widetilde{\nu})$ is static (does not slide in time), but the input to the filter, the chirp spectrum $C_{in}(\widetilde{\nu})$, now depends on both the input field and on the cavity.

In general, the interpretation of $\mathcal{E}(t)$ under coherent inputs is more simple in the sliding filter picture, as the output of a single-frequency component is $T(\nu, t)e^{j2\pi\nu t} = F(\nu - \gamma_0 t)e^{j2\pi\nu t}$ [7]. In turn, a CW FSF laser is a regenerative amplifier fed by the ASE generated in the gain section, and therefore is seeded by an incoherent input field. In this case, the output is straightforwardly described by the MC model as follows. Let us denote by $\Gamma_{in}(\tau) = \langle \mathcal{E}_{in}(t)^* \mathcal{E}_{in}(t + \tau)\rangle$ the stationary autocorrelation of the ASE field, where the brackets stand for statistical average and the asterisk for complex conjugation. It is not difficult to show from (5) that $\langle C_{in}(\widetilde{\nu}_1)^* C_{in}(\widetilde{\nu}_2)\rangle \propto \Gamma_{in}((\widetilde{\nu}_1 - \widetilde{\nu}_2)\tau_c/f_s)$, and so the amplitudes (8) are mutually incoherent provided that the coherence time of the input field is $\ll 1/f_s$. In the case of self-injection with ASE, this condition is fulfilled since it translates into the requirement that the emission's spectral width is $\gg f_s$. CW FSF laser emission is therefore understood as an incoherent moving comb, and thus without FP mode structure, continuously created from ASE and regeneratively amplified in the FS cavity. The final picture in the ν_i vs. t plane is depicted in Fig. 2(c) [36].

4. Dynamical regimes

Our first task was the identification of the different dynamical regimes arising at integer, rational, and (approximately) irrational values of the product $f_s \tau_c$ for increasing values of loop's transparency. In these experiments we used our default cavity with $\tau_c = 98.4$ ns. The identification was done by observing the output intensity in a low-bandwidth (200 MHz) oscilloscope and by measuring the FSL output power and spectra. Starting with the integer value $f_s \tau_c = 8$, we present in Fig. 3(a) the output power and in (b) the corresponding optical spectra for the different dynamical regimes. Focusing first in the output power curve we found, with increasing loop transmittance, CW emission due to ASE recirculation (blue points), QS self-pulsing emission (orange points), and ML emission at a repetition rate equal to the cavity FSR, 10.16 MHz (magenta points). In Fig. 3(c) we also present the optical spectra for an approximately irrational value of the product $f_s \tau_c = 7.675\dots$ obtained when the shifting frequency was set to 78 MHz. The analysis for both values of the $f_s \tau_c$ product will be presented in parallel since the power trace for the irrational product is similar to that in Fig. 3(a) except for the absence of the ML regime.

Below threshold recirculation is small and the CW output is broadband ASE filtered by the FBG, as shown by the smooth, light blue traces at the bottom of Figs. 3(b) and (c). Near threshold, the onset of significant recirculation is manifested in an increase of the output power and in the generation of a small, asymmetric peak in the spectrum at the FBG center frequency (middle blue traces in Figs. 3(b) and (c)). At threshold, the optical power undergoes a sudden increase that initiates a saturation trend due to the progressive compression of the amplifier's gain. The spectrum clearly reflects the expected asymmetric ASE peak, which is progressively blueshifted with respect to the FBG center as transparency increases. Representative traces are those shown in dark blue in Figs. 3(b) and (c). At the maximum output power in the CW regime, the FWHM of the emission's peak is 0.140 nm. As this peak is at threshold, one can infer from it the width of the filter that is above threshold (41.5 GHz), which amounts to ~500 recirculations.

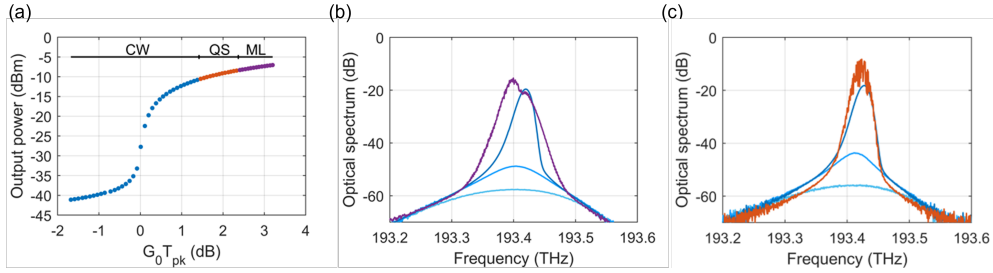At 1.5 dB above transparency, QS pulses are spontaneously built as sustained relaxation

Fig. 3. (a) Output power as a function of relative transparency, in dB, for the different regimes: blue, CW; orange, QS; and magenta, ML. (b) Optical spectra of emission at exact resonance conditions $f_s\tau_c = 8$. Blue traces: CW emission, from bottom to top, below threshold, approximately at threshold, and ~1 dB above threshold. Magenta trace: ML emission ~3 dB above threshold. (c) Same as (b) for approximately irrational values of the $f_s\tau_c$ product (f_s = 78 MHz), except for orange trace: QS emission ~3 dB above threshold. The colors in (b) and (c) correspond to the different regimes in (a).

oscillations with increasing repetition rate, in the range 12-16 kHz. The typical optical spectrum for QS emission is depicted only for irrational $f_s\tau_c$ (Fig. 3(c), blue trace), as QS emission states for $f_s\tau_c = 8$ were too close to the ML onset to provide a representative trace. This spectrum still presents the blueshifted peak, indicating that the QS pulses are built from recirculating ASE. We observe, however, that the peak is centered at lower frequencies as compared to CW emission, and also that the spectrum entails a smoother high-frequency edge. To explain this effect, let us briefly describe the QS dynamics as simulated in [16].

A time-varying spectrum is formed from ASE spontaneously generated at the FBG reflectivity peak and then moves in the direction of the frequency shift. Since the center of the filter is above threshold, amplified recirculation results in a spectral avalanche that moves towards high frequencies. Eventually, the increase in power of the amplified recirculating ASE saturates the amplifier, gain decreases, and the high-frequency end ν_+ of the net gain region progressively becomes below threshold. The ASE avalanche weakens and smoothly dies out. This is the origin of the smooth high-frequency spectral edge of the blue trace in Fig. 3(c) as compared with the CW (orange) trace. When the avalanche ceases, the loop is below threshold and the saturated gain recovers. The cycle starts again from the ASE generated at the filter's peak. Note that this view implies that the QS pulses are chirped, i.e., the central frequency of the optical spectrum varies in time in the direction of the frequency shift as the QS pulse intensity evolves. When the QS pulse dies out, the central frequency moves back towards the FBG peak where the following QS pulse is created from ASE. This chirp of the central frequency will be explicitly checked in Section 6, and contrasts with the behavior of a conventional QS laser. There, the pulse is created by the release of the energy stored by the population inversion, switched by the cavity's Q factor through active or passive means. In this case, the emission has essentially the same central wavelength along the whole QS pulse, and corresponds to the center of the spectral region where the population inversion is stored.

For $f_s\tau_c = 8$ and with increasing transparency we could induce a transition from QS to ML after generating a small perturbation in the system through a variation in f_s. In the example presented in Fig. 3(a) the transition was reached 2.4 dB above transparency, but in some cases ML emission could be started even at lower values. In general, the ML regime in FSF lasers is characterized by a pronounced hysteresis with respect to the pump power [14]; in our case, once ML pulses are formed, the transparency could be decreased down to approximately the QS onset while preserving the ML emission. ML states otherwise follow the same, smooth increasing trend in output power; we obtained a maximum value of −6 dBm at the highest available RF

power. For irrational $f_s\tau_c$ the trend in power is similar, but supported only by QS states. As can be observed in the blue trace of Fig. 3(b), the emergence of ML emission is accompanied with the appearance of a double peak in the optical spectrum [17, 21], a structure that will be analyzed in detail in Section 8.

We subsequently changed the shifting frequency f_s to fulfill additional integer ($f_s\tau_c = 7$) and fractional ($f_s\tau_c = 15/2, 22/3$ and $23/3$) conditions. The full set of emission states (CW, QS, and ML) was identified only for $f_s\tau_c = 7$ and $15/2$, whereas for $f_s\tau_c = 22/3$ and $23/3$ we only observed the transition from CW to QS. In the case of $f_s\tau_c = 15/2$ the transition from QS to ML was, however, more difficult to induce. The spectra of the different regimes showed the same features as those described in Figs. 3(b) and (c).

5. EDFA dynamics

The role of the EDFA dynamics and its saturation were analyzed in a specific set of additional experiments in our default cavity of $\tau_c = 98.4$ ns. First, we used a weak probe wavelength, with power -25 dBm at the EDFA input, to monitor its instantaneous gain in the three regimes observed for $f_s\tau_c = 8$. The measurements were performed with the low-bandwidth oscilloscope triggered by the pulses in the FSL output port and a synchronous recording of the probe power at the FBG port of Fig. 1(a). The results are shown in Figs. 4(a)-(e) for the respective emissions in CW, QS, ML, QML and HML regimes, these last two being induced by means of a procedure discussed in Section 8. By QML we refer to a ML state showing a slow, Q-switched envelope in the form of pulses which is originated by the amplifier's dynamics. The gain, shown in blue in the upper part of the corresponding plots, is presented as a relative value with respect to its mean, whereas the synchronous envelope of the intensity is plotted below in gray without scale. The intensity of ML, QML, and HML is composed of pulses at a repetition rate equal to the cavity's FSR, 10.16 MHz, which are not resolved in the corresponding plots.

As for CW, the EDFA gain shows small variations due to the intensity variations, and evolves into a switching curve in the self-sustained QS regime similar to that of passive Q-switching with a slow saturable absorber [40], with peak-to-peak gain variations of ~2% with respect to the average gain. This is in agreement with the simulated behavior in [16], where peak-to-peak relative gain variations of ~1% were found. Note also that Fig. 4(b) demonstrates that the EDFA gain presents small variations at rates of ~12 kHz. Since the QS state built as self-sustained relaxation oscillations (RO) [9], this rate coincides with the RO frequency observed when the FSF laser is suddenly turned on by switching the RF power driving the AOFS. As pointed out in [16], this contrasts with the typical upper state lifetime of Er^{3+} in silica, $\tau_2 \simeq 10$ ms when pumped at ~980 nm, a scale that is not sufficiently fast to respond to that repetition rate. This apparent contradiction is resolved by noticing that the relevant timescale in the EDFA gain dynamics is the gain's recovery time after a saturating input [41], also referred to as the effective lifetime τ_e [42]. This scale depends on τ_2, the actual pump power P_p, and the pump power for the doped fiber's transparency P_t, as $\tau_e = \tau_2/(1 + P_p/P_t)$. Under typical pumping conditions such as that used here, P_p/P_t ~10, τ_e lies in the sub-ms scale [43–46], and thus allows for small gain variations at the observed rate.

In the ML regime the amplifier cannot follow the fast repetition rate and the gain only shows slow variations due to envelope's fluctuations, as in CW. QML, as QS, is accompanied by small, synchronous changes of the instantaneous gain. The gain of HML, in turn, is almost constant due to the absence of envelope variations. This result confirms the expected behavior: the emergence of the self-pulsing QS and also of the QML emission is dictated by the EDFA relaxation dynamics, whereas CW, ML, and HML regimes encompass a nearly constant value of the gain.

In a second experiment we monitored the average EDFA gain with increasing transparency, both at integer $f_s\tau_c = 8$ and at approximately irrational values of the $f_s\tau_c$ product. Here we present the results for the first case, as both were similar. We activated the weak probe wavelength
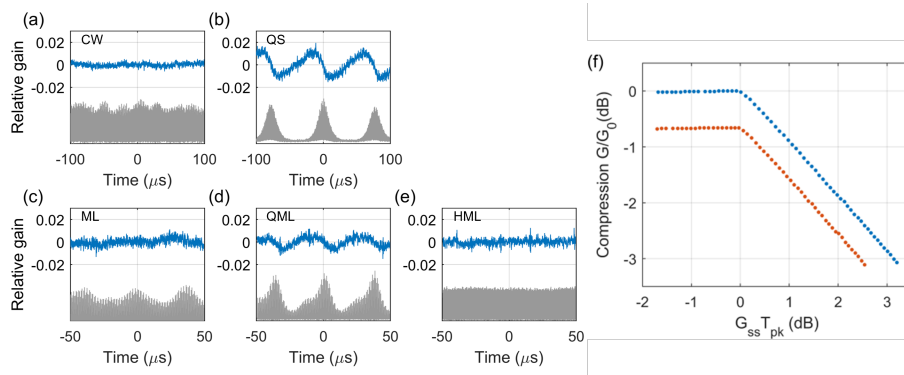
Fig. 4. Instantaneous EDFA gain (blue) and synchronous intensity (gray) of different types of emission (a) CW above threshold, (b) QS, (c) ML, (d) QML, and (e) HML. (f) EDFA compression with respect to the unsaturated gain (G/G_0) as a function of relative transparency at the FBG peak, $G_{ss}T_{pk}$, in dB. Blue trace: unsaturated amplifier. Orange trace: amplifier slightly saturated by a -13 dBm probe wavelength.

(-25 dBm) and measured its average power P_{out}^{probe} after the EDFA at the FBG transmission port by use of an OSA, not shown in Fig. 1(a). Under this weak probe power the EDFA does not suffer from compression and operates at the unsaturated gain $G_0 = 17.2$ dB. When the transparency is low, $T_{pk} \ll 1$, the power of the recirculating ASE is also low, so it does not saturates the EDFA either. In this situation, the small-signal EDFA gain coincides with the unsaturated gain, $G_{ss} = G_0$. As we increase transparency, however, the recirculating ASE may saturate the amplifier, which in general operates at a gain G.

We measured the probe power P_{out}^{probe} with increasing transparency, and normalized it by its value when $T_{pk} \ll 1$: the quotient thus represents the compression ratio $G/G_{ss} = G/G_0$ induced by ASE recirculation. The results of this measurement are shown with a blue trace in Fig. 4(f) as a function of the relative transparency $G_{ss}T_{pk}$. We observe that, after threshold, gain becomes clamped to $G \simeq T_{pk}^{-1}$ in all the emission regimes. Subsequently, the probe power was increased up to -13 dBm to describe a scenario where the amplifier is compressed by the recirculation of an externally injected field. The results are also shown in Fig. 4(f), now with an orange trace. When the saturating probe field was activated, the small-signal gain G_{ss} becomes compressed by 0.66 dB with respect to the unsaturated gain G_0. This compression level is maintained up to the threshold; after this point, recirculating ASE induces an additional saturation in the EDFA, whose gain becomes clamped again.

We mention that these results indicate that gain dynamics and intraloop power are decoupled below threshold, allowing for an effective description of the loop in terms of a constant gain. This provides an experimental justification of the standard analysis technique of FSL in signal processing applications [47,48]. It should be pointed out, however, that the existence of saturation below threshold cannot be discarded in general but, of course, would involve the use of amplifiers with a relatively high noise figure together with filters of large spectral width. The global picture inferred from Fig. 4(f) is thus to be considered as representative for a standard FSL implementation.

6. Q-switched pulses

In this section we address the characterization of two features of the QS pulses that seem not to have been documented in the literature, leaving the detailed study of the ASE recirculation patterns for the following section. As a representative example, we set the frequency shift at

approximately irrational conditions (f_s = 78 MHz) in a loop with roundtrip time τ_c = 107.8 ns.

In Fig. 5(a) we present a high-bandwidth (6 GHz, 20 GSa/s) intensity trace of a typical Q-switched pulse generated 3 dB above threshold. The pulse's repetition rate was in this case 14.252 kHz and its FWHM, 9.5 μs. As can be observed, the pulses present a symmetric sech^2 profile with spiky features, which are organized in a quasiperiodic structure repeated at the cavity's roundtrip time. A zoom view of 10 recirculations from the peak of a typical QS pulse is presented in Fig. 5(b). A similar quasiperiodic structure was found in the QS regime of Ti:sapphire FSF lasers [14], and also appears when the AOFS is removed from the FS cavity [17]. We thus interpret this quasiperiodic pattern as a consequence of the recirculation of ASE events: at a given time, the intensity is dominated by the waves that flow near the high-frequency end ν_+ of the net gain region, so that they can recirculate several times without significant gain or attenuation. Intensity is then observed as a random but quasiperiodic pattern with periodicity τ_c, that is adiabatically refreshed with new waves that were originated at the low-frequency end ν_- of the cavity's net gain region and amplified upon recirculation.
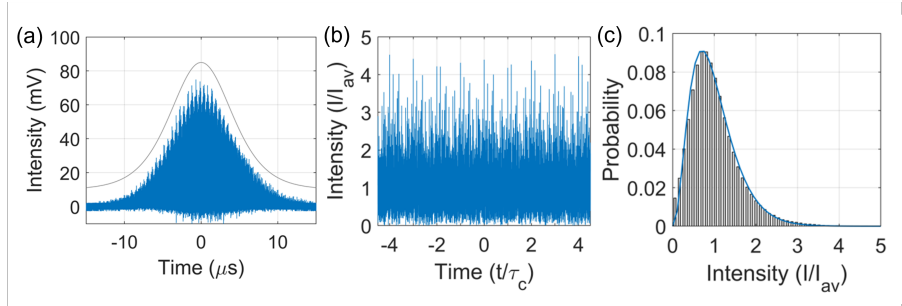

Fig. 5. (a) Intensity of a QS pulse. Gray trace: sech^2 profile, shifted upwards to ease the comparison. (b) Quasiperiodic intensity, relative to the mean intensity, extracted from the peak of a typical QS pulse. (c) Intensity probability density: Histogram, experimental data. Blue trace: Gamma distribution with m = 3.4. In (b) and (c) the cavity's roundtrip time was τ_c = 98.4 ns.

To check this hypothesis, we estimated the intensity distribution of the quasiperiodic pattern as follows. We first recorded the intensity in a time span comprising the ~200 central roundtrips around the QS pulse peak, where the electrical noise contribution from the photodiode is relatively low. The intensity trace was then normalized by a moving mean, averaged over a roundtrip. The distribution of the resulting relative intensity was then estimated by a histogram. As is well known, the intensity of polarized ASE observed in a finite bandwidth B is described by a Gamma distribution, $p_m(x) = m^m x^{m-1} \exp(-mx)/\Gamma(m)$, where x is the intensity I relative to its average I_{av} and m a parameter that is roughly the ratio between the ASE spectral width $\Delta\nu$ and the observation bandwidth B = 6 GHz [51]. Under typical conditions, the FWHM of the QS spectrum is about 0.15 nm, so we estimate $m \sim 3$. The result of the comparison in Fig. 5(c) shows an excellent agreement. The best fit is attained for m = 3.4, in accordance with the estimation.

We also show that these ASE events constitute a noisy pattern that univocally identifies each pulse in the sequence, as can be inferred from an analysis of the intensity correlation between different pulses. First, a high-bandwidth trace of the intensity of five consecutive pulses was recorded. From this trace, the intensity of the central pulse, taken as the reference pulse, was isolated, and then digitally correlated with the complete sequence of five pulses. The result is shown Fig. 6(a). The central part of the figure thus represents the intensity auto-correlation of the reference pulse, whereas the remaining peaks represent the intensity cross-correlation of the reference pulse and its neighbors. This intensity cross-correlation is composed of smooth peaks, indicating that the ASE spikes between different pulses are statistically uncorrelated because

ASE recirculation is switched off between pulses. In turn, the intensity auto-correlation of the reference pulse with itself shows additional peaks at multiples of τ_c, as is clearly visible in the zoom view of Fig. 6(b).
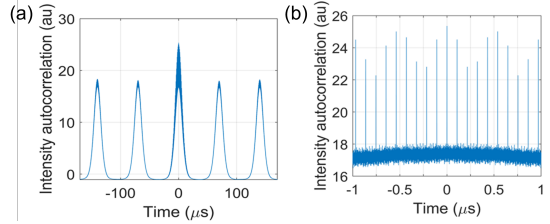

Fig. 6. (a) Intensity cross-correlation of a reference pulse with the pulse sequence. (b) Zoom of the intensity auto-correlation of the reference pulse.

In a subsequent experiment we characterized the motion of spectral density's central frequency by a time-frequency reconstruction of the QS pulse. To this end, we inserted a Mach-Zehnder intensity modulator (MZM) at the FSL's output acting as a temporal switch. The MZM switching signal was generated by a programmable pulse generator and triggered by the pulse detected at the transmission port of the FBG. Representative traces of this procedure are shown in Fig. 7(a). The average spectrum of each of the samples was subsequently retrieved in a OSA. The resulting time-frequency reconstruction is depicted in Fig. 7(b), where it is apparent the pulse's positive chirp and the flow of the spectral density towards lower frequencies at its trailing edge.
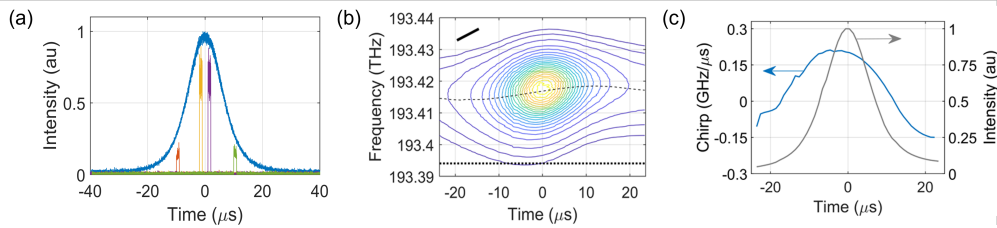

Fig. 7. (a) Temporal samples of width 1 µs (orange, yellow, magenta, and green traces) used in the time-frequency reconstruction of the QS pulse (blue trace). (b) Time-frequency contour plot of a QS pulse. The dotted trace is the time-varying ASE center frequency $\nu_0(t)$. The dotted line at 193.394 THz is the FBG center frequency. The black line in the left upper corner represents the natural chirp rate γ_0 of the FS cavity. (c) Pulse chirp $d\nu_0/dt$ (blue) and pulse intensity (gray).

From this plot we extracted the center frequency $\nu_0(t)$ of the moving spectrum and plotted its evolution $d\nu_0/dt$ in Fig. 7(c). In this last figure we also depict the synchronous pulse intensity obtained by projecting in time the total pulse power in the two-dimensional plot of Fig. 7(b). The existence of chirp is clearly captured, with a maximum value of $\gamma = 0.20$ GHz/µs slightly before the pulse's peak. The measured chirp rate γ is lower than the cavity's natural rate, $\gamma_0 = f_s/\tau_c = 0.72$ GHz/µs, a rate that has been added in the upper left corner of Fig. 7(b) with a black line to help the comparison. This feature is a consequence of the pulse buildup as an avalanche of recirculating ASE events, on-off switched by the EDFA dynamics: the actual chirp rate γ of the central frequency is a spectral average that depends not only on the chirp rates γ_0 of the individual ASE events, but also on the frequency and time when these ASE events are generated.

7. ASE recirculation patterns in CW and QS regimes

The ASE recirculation in CW and QS regimes shows interesting intensity patterns that depend on the actual value of the $f_s\tau_c$ product. We found that these patterns are similar in both regimes for the same value of $f_s\tau_c$, indicating that its origin is due to the ASE recirculation process and not to the QS pulse dynamics. In Fig. 8 we present, in the first column, the different patterns appearing inside the QS pulses, for which the high SNR at the pulse's center permits a clear visualization. We stress, however, that the ASE recirculation patterns in CW emission are qualitatively similar to those of QS emission for the same values of $f_s\tau_c$. The central column depicts the RF intensity spectra in CW emission, whereas the spectra in the right column refers to QS emission, so that their differences can be comparatively analyzed. These experiments were performed in our default cavity of $\tau_c = 98.4$ ns.
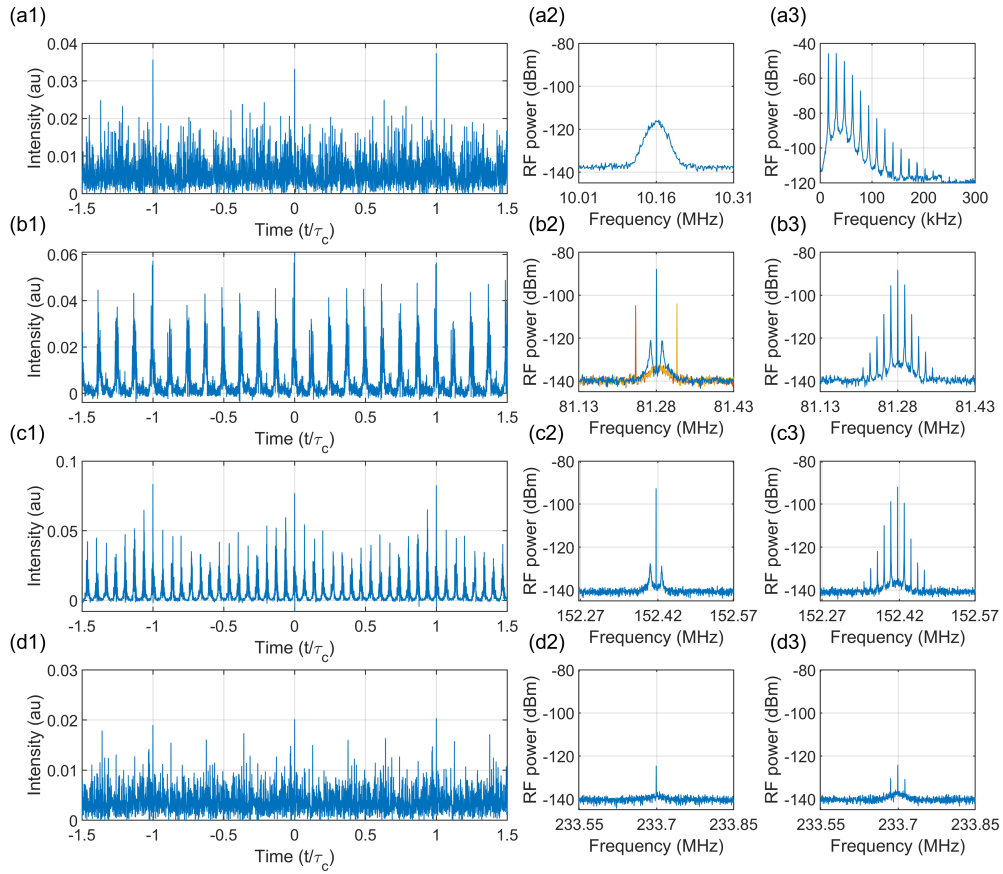

Fig. 8. Left column: intensity patterns of ASE recirculation in QS regime for different values of the $f_s\tau_c$ product: (a1) approximately irrational product ($f_s = 78$ MHz, $\tau_c = 98.4$ ns), (b1) resonant integer product $f_s\tau_c = 8$, (c1) resonant fractional product $f_s\tau_c = 15/2$, and (d1) resonant fractional product $f_s\tau_c = 23/3$. Middle column: RF intensity spectrum of the corresponding CW regimes measured at the cavity fundamental (a2) and at the cavity p-th harmonic for integer or fractional products $f_s\tau_c = p/q$ (b2-d2). In (b2) two almost resonant products are also shown (orange and yellow traces). Right column: RF intensity spectrum of the QS regimes measured at baseband (a3) and at the cavity p-th harmonic (b3-d3). All RF spectra were taken at an IF bandwidth of 30 Hz.

As is shown in Fig. 8(a1), at an approximately irrational value of $f_s\tau_c$ ($f_s = 78$ MHz), the intensity of the recirculating ASE appears as the quasiperiodic pattern discussed before. In Fig. 8(a2) we present the RF spectrum of the CW intensity at the cavity's fundamental harmonic of 10.16 MHz. The spectrum at the other harmonics is similar in width but with decreasing amplitude. According to the MC model of recirculation, the observed RF peak represents the aggregate spectrum of the incoherent optical beats between consecutive chirps of indices k and $k + 1$. Its width (24 kHz FWHM) is thus $\sqrt{2}$ times the spectral width $\Delta\widetilde{\nu}$ of the amplitudes $A_k(t)$ in (7). Similar spectra appear at the output of a Michelson interferometer when fed with CW FSF laser light [36]. Since the complex amplitude's bandwidth is induced by the filtering capacities of the loop, one can ascribe an effective finesse to the active FS cavity given by $\mathcal{F} = \text{FSR}/\Delta\widetilde{\nu} = 10.16$ MHz$/17$ kHz $= 600$, of the order of the number of roundtrips necessary to cross the filter when the loop is above threshold. Finally, in Fig. 8(a3) we present the baseband spectrum of the intensity in the QS regime (excluding the dc level), where the harmonics at the QS repetition rate (15.65 kHz) are apparent.

The ASE intensity patterns arising when the frequency shift is near resonant products $f_s\tau_c = p/q$ are shown in Fig. 8(b1) and (c1) for the respective cases of 8 and 15/2. The plot evidences that ASE recirculation is organized in a series of ASE pulses with a respective periodicity of f_s and $2f_s$ that amounts to 8 and 15 pulses per roundtrip, respectively. The height of the pulses within each roundtrip is not uniform, and changes adiabatically in the same experiment and also from one experiment to another. The ASE intensity pattern also shows up as a sharp tone in the RF intensity spectra of CW emission at the corresponding 8th and 15th FSR harmonics, respectively, as is shown in (b2) and (c2). In (b2) we varied f_s around $8/\tau_c = 8$ FSR, revealing that the tone is stimulated most at the exact resonant value. At this exact resonant conditions we also observed that the form of the ASE pulses are sharper. We checked that, as f_s departs from the resonance, the tone progressively disappears, the periodic intensity pattern becomes smoother and, when the mismatch $\delta f = qf_s - p/\tau_c$ substantially departs from $\Delta\widetilde{\nu}$, becomes random-like and thus similar to that of Fig. 8(a1). The noise skirts around f_s at the exact resonant condition (in blue in (b2) and (c2)) are due to the excitation of relaxation oscillations in the EDFA. These skirts become tones when the FSL reaches the QS regime, as is shown in (b3) and (c3). This periodic ASE recirculation pattern was identified in [13] in a linear-cavity Er:fiber FSF laser in both CW and QS regimes at the resonant product $f_s\tau_c = 10$, but its origin as a form of ASE recirculation was not recognized. We also point out that the same periodic organization in pulses is obtained when the loop is seeded with a monochromatic carrier [49, 50]. In this case, however, the pulses are not composed of recirculating ASE, but are created through temporal Talbot effect and are thus optically coherent.

In the fourth row of Fig. 8 we depict the results for $f_s\tau_c = 23/3$. Here, we observe in (d1) that the intensity is similar to an irrational value of the product $f_s\tau_c$ despite the fact that the expected tone at $3f_s$ is present at the 23th cavity harmonic, both in CW (d2) and QS (d3) regimes. However, the tone is too weak to produce discernible features in the intensity trace. Finally, products $f_s\tau_c = p/q$ in the available range with $q > 3$ (not shown in the figure) did not show any perceptible trace of the tone at qf_s.

These results point to the existence of a phase locking mechanism among recirculating waves whose instantaneous frequencies differ by qf_s. Such a mechanism has to be effective only in the vicinity of resonant products $f_s\tau_c \simeq p/q$. This can be explained from the MC model of ASE recirculation as follows. In this model, any pair of chirped waves in (7) with indices differing by p units can support, if phase-locked, the observed periodic intensity pattern at the frequency difference qf_s, since in that case $\widetilde{\nu}_{k+p} - \widetilde{\nu}_k = p/\tau_c \simeq qf_s$ for any k. This is schematically exemplified in Fig. 9 for $f_s\tau_c = 2$. In order for the FS cavity to be able to support such pairs of locked chirps, the frequency mismatch δf must lie within the $\Delta\widetilde{\nu} \sim 17$ kHz bandwidth of each of the chirp's amplitudes. Also, at exact resonant conditions $qf_s = p/\tau_c$ (and in the absence of
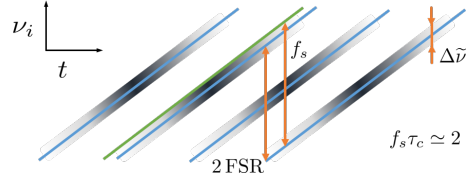
Fig. 9. Schematics of the ν_i vs. t plane near the resonant condition $f_s\tau_c \simeq 2$, showing four chirped waves. The center difference between the instantaneous frequencies of next-to-neighbor chirps is $2\,\mathrm{FSR} = 2/\tau_c$ (blue lines). Coupled chirps with frequency difference $f_s \simeq 2\,\mathrm{FSR}$ can recirculate in the FS cavity due to the finite spectral width $\Delta\widetilde{\nu}$ of the recirculating chirps (blue and green lines).

significant dispersion), the locked chirps could form larger groups with indices k, $k \pm p$, $k \pm 2p$, ... resulting in sharper ASE pulses. All these implications are in accordance with the observed phenomenology.

This view, however, has its limitations. First, it does explain the weakening of the effect when $q \geq 3$. Second, when $p > 1$ several locked groups of chirps with indices differing by p units can be independently formed. The intensity would then be an incoherent sum of periodic patterns associated to each group of chirped waves, and the temporal coincidence among different patterns cannot be assured unless we assume a phase locking between groups of chirps, or the preeminence of a single group of chirps. Otherwise, the periodic patterns in Figs. 8(b1) and (c1) would be washed out. And third, within a framework of ASE recirculation in a linear cavity there is no mechanism for the alleged phase locking among chirped waves. At this point it is necessary to recall the results of [22], where the tone at f_s was identified in the RF intensity spectrum of a MIR FSF laser based on a Ho/Pr-doped ZBLAN gain fiber section, mode-locked near the resonant product $f_s\tau_c \simeq 1$. In this regard our results show that the presence of this tone is not associated to any dynamical effect within the ML regime, but to the ASE generation and recirculation processes. The ML dynamics, however, is influenced by this pattern as will be analyzed later.

As for the possible coupling mechanism, in [22] it was suggested the existence of a residual frequency modulation in the AOFS, a hypothesis that could be certainly translated to our setup despite the different architectures involved. A second possibility is that alleged in [32] to justify the preeminence of groups of chirps with increasing pump power, namely a coupling induced by Kerr effect, presumably through four-wave mixing among different chirped waves when they are spontaneously created at the low-frequency end ν_- of the net gain region. These coupled chirps would then get amplified, arriving at the high-frequency end ν_+ in the form of the observed pattern.

8. Modelocked emission

Well above threshold and both at integer and fractional values of the product $f_s\tau_c = 7, 8$ and $15/2$, ML emission emerges as a series of pulses with a periodicity dictated by the cavity's rountrip time. As is typical of FSF lasers at large gain [17, 20], ML pulses appear in the form of a cluster grouped here in a sub-ns interval, as is shown in Fig. 10(a) for $f_s\tau_c = 8$, the default situation in the present section. The resolution of this plot does not provide an evidence of this multipulse state, but can be indirectly inferred if one decreases the pump power or the loop's transmittance. In this case, it is observed how pulses leak, i.e., are adiabatically ejected from the cluster and die out [17], eventually ending in a single, sub-ns pulse as that shown in Fig. 10(b).

For the analysis of the ML emission we first refer to the optical spectrum in Fig. 3(b) and to the first row of plots in Fig. 11(a1)-(a4). The ML spectrum in Fig. 3(b) is characterized by the
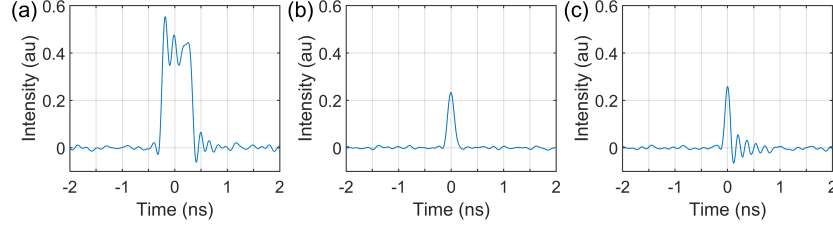
Fig. 10. (a) High-bandwidth (6 GHz) intensity trace of the multipulse cluster state in the ML regime at exact resonant conditions $f_s \tau_c = 8$ and maximum transparency (~3 dB above threshold). (b) Single ML pulse obtained from (a) after decreasing the pump power down to ~1 dB above threshold. (c) Single ML pulse ejected from the cluster (a) when the shifting frequency is detuned ~200 kHz from resonance. Experiments performed with a cavity roundtrip time of $\tau_c = 98.4$ ns.

development of a dominant spectral peak near the center of the FBG with a power higher than that of a secondary peak located at the same frequency as the recirculating ASE peak [17, 21]. We will refer to these peaks as main and secondary in what follows. This structure is known to be more visible with increasing intracavity filter bandwidth, since in that case the high-frequency end ν_+ of the net gain region and the filter's center are more apart. It is also known that the location of the secondary peak is reversed with respect to the main peak when the sign of the frequency shift is flipped [17].

A second feature, which seems to have been overlooked, is that the recirculation of ASE coexists with the ML pulses, as is evidenced in the intensity trace of Fig. 11(a1) and its inset. This pattern is more visible near the ML onset, condition under which this trace was recorded. In this setting, the difference in power between main and secondary spectral peaks is lower, as is exemplified in blue trace of Fig. 12(a). On the other hand, at longer time scales ML pulses present an irregular envelope, as depicted in Fig. 11(a2). The spectrum of these fluctuations is given by the baseband spectrum of the intensity, shown in (a3), where we observe a main resonance at ~28 kHz together with its harmonics. The fluctuations are transferred as noise sidebands to all the intensity harmonics, as can be observed in (a4) for the fundamental, where the peak-to-pedestal value is 60 dB.

The interpretation of these features is the following. We first show, through a specific experiment, that for arbitrary values of $f_s \tau_c$ the double peak in the spectrum of ML emission is associated to two different fields, the ASE recirculation which accounts to the secondary peak, and the ML field, whose spectrum extends along the whole observed spectral trace and is centered in the main peak. To this end, we take advantage of our identification of the periodic ASE recirculation pattern at resonant conditions, which is used as a probe to assess the relative power of ASE and ML pulses in different parts of the spectrum.

The FSL output at $f_s \tau_c = 8$, set about 2 dB above threshold, was directed to a narrowband tunable bandpass filter (TBF) and then detected with a photodiode in the 200 MHz oscilloscope with the aid of a transimpedance amplifier. The intensity trace was first recorded by zooming the pedestal of ML pulses, and then divided by the peak amplitude of the ML pulses under the same filtering conditions. As can be observed in Fig. 12 (blue traces in (a) and (b)), when the spectrum is not filtered both ML pulses and the ASE recirculation pattern are detected with a relative intensity of 0.35%. When the spectrum is filtered at the main peak (magenta traces in (a) and (c)), ASE does not form any definite pattern; a noisy pedestal is observed instead. The TBF center wavelength was then shifted, without change in its width, up to the secondary peak of the spectrum (red traces in (a) and (d)): we observe that the ASE recirculation pattern becomes visible again, but now with an increase in its relative intensity up to a 3% (note the
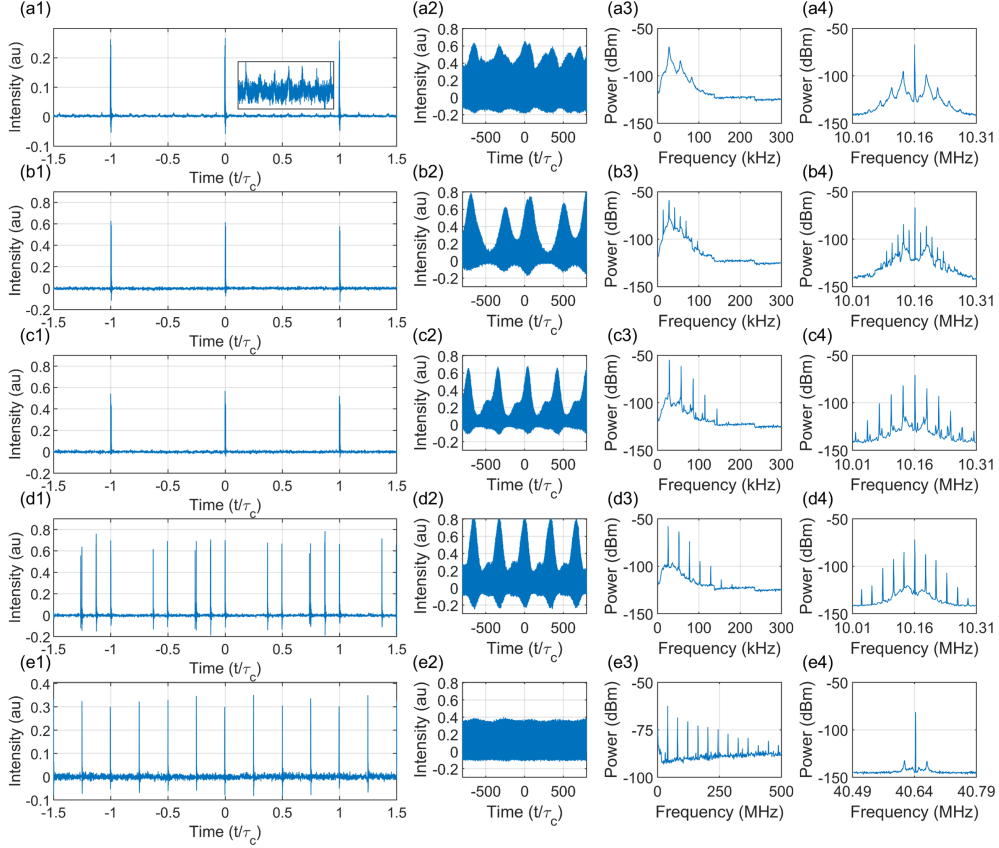
Fig. 11. Left column: high-bandwidth (6 GHz) intensity trace of different ML emission states: (a1) ML multipulse cluster at exact resonance conditions $f_s \tau_c = 8$ ($f_s = 81.286$ MHz), inset: detail of the periodic ASE recirculation pattern. (b1) emission at a mismatch $\delta f = -14$ kHz supported by a multipulse cluster. (c1) QML emission at a mismatch $\delta f = -28$ kHz, also supported by a multipulse cluster. (d1) QML emission supported by a pattern of several pulses ejected from the multipulse cluster. (e1) HML emission at a mismatch $\delta f = -3.107$ MHz. Second column: (a2)-(e2) Envelopes of the correspoding ML emission states. Third column: (a3)-(d3) Baseband spectrum of the corresponding intensities. (e3) Wideband spectrum of the HML state. Right column: (a4)-(d4) Spectrum of the fundamental harmonics of the corresponding intensities. (e4) Spectrum of the $N = 4$ harmonic in the HML state. All RF spectra were taken at a IF bandwidth of 10 Hz, except (d3) where it is 3 kHz. The cavity's roundtrip time was $\tau_c = 98.4$ ns.

change of scale). If the shifting frequency is now displaced by a few tens of kHz from the resonant condition, the periodic pattern disappears, a small noise level is observed instead, and the secondary peak in the spectrum decreases by ~2.5 dB. This shows that ASE recirculation with periodic intensity is favored at resonance. Nonetheless, the secondary spectral peak persists out of the resonance, now as a shoulder of the main peak, indicating that ASE recirculation is still present in the form of a noise-like waveform.

These results are to be compared with the recent report of the spectro-temporal structure of the ML buildup in a Er:fiber FSF laser at small frequency shifts [29]. There, it was shown that ML evolves from QS, and this evolution is accompanied with a different regime of recirculation of
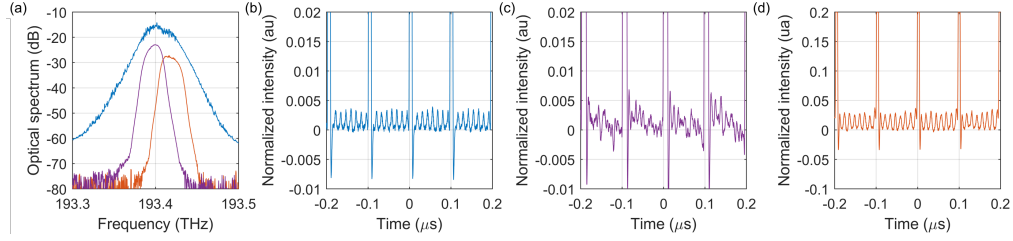
Fig. 12. (a) Blue: optical spectrum of ML emission with $f_s \tau_c = 8$. Magenta: filtered spectrum at the main spectral peak. Orange: filtered spectrum at the secondary peak. (b) Intensity of the ASE recirculation pattern between ML pulse clusters, normalized by the peak intensity of the ML cluster. (c) Normalized intensity of the ASE recirculation pattern when the emission is filtered at the main peak. (d) Normalized intensity of the ASE recirculation pattern when the emission is filtered at the secondary peak.

the fields: QS pulses appear centered at a higher frequency than ML and constituted by chirped waves. These results are in accordance with the picture inferred here. In fact, and given the data in that report ($f_s = 2 \times 1.0515$ MHz and $\tau_c = 82$ ns), the chirp rate observed in the QS regime (Figs. 3(c) and (d) in [29]) is compatible with the cavity's natural rate γ_0, as predicted by the MC model, and the downshift of the spectrum when evolving from QS to ML is similar to that reported here and in other demonstrations in regard to its double peak structure [17, 21].

As for the noisy envelope in Fig. 11(a2), it is ascribed to the excitation of relaxation oscillations in the EDFA, but now at a frequency of ~28 kHz which is roughly twice that observed in the QS regime (~14 kHz). In fact, a careful observation of Fig. 11(a3) shows that the ~14 kHz resonance is still present as a shoulder in the low-frequency skirt of the dominant noise resonance at ~28 kHz. The reason for this identification is because, following [22], we could induce QML from ML by varying the frequency shift out of the resonant value. The spectrum of the intensity, both at baseband and at the eighth harmonic, develops a modulation tone at the mismatch frequency $\delta f = f_s - 8$ FSR originated by the periodic ASE recirculation pattern.

When this mismatch is ~14 kHz, the noisy envelope becomes almost periodic but does not develop a series of well-defined QML pulses, as is shown in the plots of the second row of Fig. 11(b1)-(b4). When the mismatch becomes ~28 kHz, the ASE tone drives the EDFA relaxation oscillations and QML is induced, as is clearly observable in the third row (c1)-(c4) of Fig. 11. If the mismatch δf is further increased beyond some tens of kHz, ejection of pulses from the multipulse cluster is observed. A sample ejected pulse is plotted in Fig. 10(c). This ejection does not provide, in general, a periodic pattern of the intensity: pulses drift within each period of duration τ_c. This phenomenon has also been observed in other FSF lasers at large pump powers [20]. The envelope, however, becomes stabilized, as will be exemplified below. At this point, if ones goes back to the QML conditions, namely $\delta f \simeq 28$ kHz, a stable QML state is observed where the ejected pulses are now fixed at definite positions within period τ_c, as is depicted in plots (d1)-(d4) of Fig. 11.

The ML state in the form of a series of drifting pulses, or even in the form of QML, could be observed for values of the mismatch δf in the complete AOFS operation range 80 ± 5 MHz. In this range, ML emission shows the double peak in the spectrum. Also, a decrease in transparency in this range of f_s leads to ML states where pulses are ejected and die out, drifting within the period τ_c, as in [20]. When the frequency shift approaches $f_s \tau_c = 7$ or 15/2, the output collapses into the multipulse ML cluster of Fig. 11(a1)-(a4). At certain values of the mismatch we observed that the pulses ejected from the original cluster, say N in number, progressively became equally spaced, thus resulting in harmonic mode locking (HML). In this regard, the process of HML formation is similar to that reported in [9] or, more recently, in [21, 29]. This process has been

ascribed to the amplifier's dynamics, which favors emission in equidistant pulses as a means to equalize gain [9]. In our loop, stable HML was difficult to achieve, requiring a fine tuning of shifting frequency, loop transparency, or even the induction of a small amount of compression in the EDFA through the probe wavelength.

A typical HML state obtained this way is exemplified in Fig. 11(e1)-(e4) for $N = 4$, where the peak-to-pedestal value of the fourth harmonic in (e4) is 64 dB. Note that here (e3) is the wideband spectrum of the intensity displaying the locked harmonics at multiples of 40.64 MHz, and (e4) is the zoom view of the fourfold increased fundamental. Also, the stabilized intensity envelope shown in (e2) is representative of all envelopes out of the vicinity of resonances. Using this procedure, we could induce HML with different degrees of stability for various values of $N \leq 11$, as was originally reported in [9]. The order N of the obtained HML depends on the number of ejected pulses of the original cluster, and so on the actual value of the transparency upon which the initial ML multipulse cluster is formed.

9.   Conclusions

A systematic characterization of the different pulsed dynamical regimes of an Er:fiber FSL at large frequency shifts has been presented, and connection with different results in the literature has been provided. The main findings can be summarized as follows. Within the QS regime, we have shown the intrinsic tagging of individual QS pulses through the intensity of the underlying ASE recirculation patterns and the demonstration of its chirped character as predicted in [16]. A specific periodic recirculation mode of ASE near resonant conditions has been identified in both CW and QS regimes, previously interpreted as a pulsed regime without reference to its origin as an ASE recirculation mode [13]. The phenomenology associated with this ASE recirculation regime has been shown to be partially explained through the MC model of ASE recirculation [36], which has been presented here as a static FP filter for the first time. As for the ML regime, it has been induced from resonant FS cavities at fractional values of the product $f_s \tau_c$. It has been clarified the origin of the double peak structure of the ML FSF laser spectrum [17, 21], and connection has been established with recent results describing the spectro-temporal structure of the ML buildup process in FSF lasers at small frequency shifts [29]. It has also been shown that, near resonant conditions, recirculating ASE in the form of a periodic intensity drives the QML emission by inducing relaxation oscillations, this being the cause of the phenomenology described in [22].

The global picture arising from these results can also be summarized as follows. With increasing transparency, FSF laser emission evolves from CW to QS due to the amplifier's dynamics, the supporting optical fields being in both cases recirculating ASE. At and near resonant conditions ASE takes the form of a periodic intensity pattern, presumably due to Kerr interactions between the chirped waves described by the MC model [32]. The transition from QS to ML is also ascribed to Kerr effect, which generates a phase distribution throughout the optical spectrum [9]. Since in the time domain a moving comb of chirped waves of the form (7) with fixed relative phases leads to ML pulses [32], it is thus expected that the ML buildup is favored at resonant cavities because of the previous coupling of these chirped waves, this being a possible justification for the lower ML threshold pump power at resonance [20]. ML is also accompanied with a change in the spectral shape that moves to the high-gain region at the filter's peak. But the underlying ASE recirculation persists in the form of a small perturbation, reflected in the secondary peak of the spectrum. This opens the possibility to reduce the ASE level by filtering this secondary peak. When the cavity is near the resonant value, ASE recirculation drives the ML state, in particular inducing QML. ML emission shows typically as a cluster of pulses, and also with a prominent hysteresis in pump power or transparency. Pulses are forced to be ejected from the cluster by changes in transparency or shifting frequency over broad frequency ranges, and HML results when these ejected pulses are stabilized at equal time intervals.

In conclusion, our study has clarified the role of the underlying ASE recirculation in the origin of various spectral and dynamical properties of pulsed FSF lasers. It has also pointed to the existence of specific mechanisms that deserve further study, such as the development of periodic ASE patterns at resonant conditions and the rich ML dynamics leading to QML and HML. Though our findings have been derived from a Er:fiber FSL, the number of related results described in the literature, comprising different lasing media and cavity configurations, indicate that these features are at the root of the dynamics of pulsed FSF lasers.

Disclosures. The authors declare no conflicts of interest.

Data availability. Data underlying the results presented in this paper are not publicly available at this time but may be obtained from the authors upon reasonable request.

References

1. D. J. Taylor, S. E. Harris, and S. T. K. Nieh, "Electronic tuning of a dye laser using the acousto-optic filter," Appl. Phys. Lett. **19**(8), 269-271 (1971).
2. F. V. Kowalski, P. D. Hale, and S. J. Shattil, "Broadband continuous-wave laser," Opt. Lett. **13**(8), 622-624 (1988).
3. F. V. Kowalski, S. J. Shattil, and P. D. Hale, "Optical pulse generation with a frequency shifted feedback laser," Appl. Phys. Lett. **53**(9), 734-736 (1988).
4. P. Myslinski, J. Chrostowski, J. A. K. Koningstein, and J. R. Simpson, "High power Q-switched erbium doped fiber laser," IEEE J. Quantum Electron. **28**(1), 371-377 (1992).
5. F. V. Kowalski, J. A. Squier, and J. T. Pinckney, "Pulse generation with an acousto-optic frequency shifter in a passive cavity," Appl. Phys. Lett. **50**(12), 711-713 (1987).
6. P. D. Hale and F. V. Kowalski, "Output characterization of a frequency shifted feedback laser: Theory and experiment," IEEE J. Quantum Electron. **26**(10), 1845-1851 (1990).
7. H. Guillet de Chatellus, E. Lacot, W. Glastre, O. Jacquin, and O. Hugon, "The hypothesis of the moving comb in frequency shifted feedback lasers," Opt. Commun. **284**(20), 4965-4970 (2011).
8. H. Sabert and E. Brinkmeyer, "Stable fundamental and higher order pulses in a fibre laser with frequency shifted feedback," Electron. Lett. **29**(24), 2122-2124 (1993).
9. H. Sabert and E. Brinkmeyer, "Pulse generation in fiber lasers with frequency shifted feedback," J. Lightw. Technol. **12**(8), 1360-1368 (1994).
10. Y. Kodama and S. Wabnitz, "Analysis of soliton stability and interactions with sliding filters," Opt. Lett. **19**(3), 162–164 (1994).
11. F. Fontana, L. Bossalini, P. Franco, M. Midrio, M. Romagnoli, and S. Wabnitz, "Self-starting sliding-frequency fibre soliton laser," Electron. Lett. **30**(4), 321–322 (1994).
12. C. Martjin de Sterke and M. J. Steel, "Simple model for pulse formation in laser with a frequency-shifting element and nonlinearity," Opt. Commun. **117**(5-6), 469-474 (1995).
13. I. R. Perry, R. L. Wang, and J. R. M. Barr, "Frequency shifted feedback and frequency comb generation in an Er^{3+}-doped fibre laser," Opt. Commun. **109**(1-2), 187-194 (1994).
14. G. Bonnet, S. Balle, Th. Kraft, and K. Bergmann, "Dynamics and self-modelocking of a titanium-sapphire laser with intracavity frequency-shifted feedback," Opt. Commun. **123**(4-6), 790-800 (1996).
15. M. Stellpflug, G. Bonnet, B. W. Shore, and K. Bergmann, "Dynamics of frequency shifted feedback lasers: simulation studies," Opt. Express **11**(17), 2060-2080 (2003).
16. J.-N. Maran, P. Besnard, and S. LaRochelle, "Theoretical analysis of a pulsed regime observed with a frequency-shifted-feedback fiber laser," J. Opt. Soc. Am. B **23**(7), 1302-1311 (2006).
17. L. A. Vazquez-Zuniga and Y. Jeong, "Study of a mode-locked erbium-doped frequency-shifted-feedback fiber laser incorporating a broad bandpass filter: Experimental results," Opt. Commun. **306**, 1-8 (2013).
18. L. A. Vazquez-Zuniga and Y. Jeong, "Study of a mode-locked erbium-doped frequency-shifted-feedback fiber laser incorporating a broad bandpass filter: Numerical results," Opt. Commun. **322**, 54-60 (2014).
19. S. Balle and K. Bergmann, "Self-pulsing and instabilities in a unidirectional ring dye laser with intracavity frequency shift," Opt. Commun. **116**(1-3), 136-142 (1995).
20. W. Chen, S. P. Chen, Z. F. Jiang, and J. Hou, "Diversified pulse generation from frequency shifted feedback Tm-doped fibre lasers," Scientific Reports, **6**, 26431 (2016).
21. R. I. Woodward, M. R. Majewski, and S. D. Jackson, "Mode-locked dysprosium fiber laser: Picosecond pulse generation from 2.97 to 3.30 μm," APL Photonics **3**(11), 116106 (2018).

22. M. R. Majewski, R. I. Woodward, and S. D. Jackson, "Ultrafast mid-infrared fiber laser mode-locked using frequency-shifted feedback," Opt. Lett. **44**(7), 1698-1701 (2019).
23. R. I. Woodward, M. R. Majewski, N. Macadam, G. Hu, T. Albrow-Owen, T. Hasan, and S. D. Jackson, "Q-switched Dy:ZBLAN fiber lasers beyond 3 μm: comparison of pulse generation using acousto-optic modulation and inkjet-printed black phosphorus," Opt. Express **27**(10), 15032-15045 (2019).
24. W. Yue, T. Chen, W. Kong, C. Mou, G. Huang, Z. He, and R. Shu, R. (2022). "Spectral and repetition rate programmable fiber laser," J. Lightw. Technol. **40**(17), 5995-6000 (2022).
25. O. Henderson-Sapir, N. Bawden, A. Theodosiou, M. R. Majewski, K. Kalli, S. D. Jackson, and D. J. Ottaway, "Mode-locked and tunable 3.5 μm fiber laser using an acousto-optic modulator," J. Lightw. Technol., **41**(2), 716-725 (2023).
26. S. Jackson, R. Vallee, and M. Bernier, eds., *Mid-Infrared Fiber Photonics*. (Woodhead Publishing, 2021).
27. X. Li, X. Huang, X. Hu, X. Guo, and Y. Han, "Recent progress on mid-infrared pulsed fiber lasers and the applications," Opt. Laser Technol., **158**, 108898 (2023).
28. F. Amrani, M. Salhi, P. Grelu, H. Leblond, and F. Sanchez, "Universal soliton pattern formation in passively mode-locked fiber lasers," Opt. Lett. **36**(9), 1545-1547 (2011).
29. Z. Gao and T. Mei, "Spectro-temporal evolution of mode-locked lasing in fiber frequency-shifted feedback laser," Opt. Lett. **47**(19), 4973-4976 (2022).
30. V. Durán, H. Guillet de Chatellus, C. Schnebélin, K. Nithyanandan, L. Djevarhidjian, J. Clement, and C. R. Fernández-Pousa, "Optical frequency combs generated by acousto-optic frequency-shifting loops," IEEE Photon. Technol. Lett. **31**(23), 1878-1881 (2019).
31. L. P. Yatsenko, B. W. Shore, and K. Bergmann, "Theory of a frequency-shifted feedback laser," Opt. Commun. **236**(1-3), 183-202 (2004).
32. S. Balle, I. C. Littler, K. Bergmann, and F. V. Kowalski, "Frequency shifted feedback dye laser operating at a small shift frequency," Opt. Commun. **102**(1-2), 166-174 (1993).
33. K. Nakamura, K. Kasahara, M. Sato, and H. Ito, "Interferometric studies on a diode-pumped Nd:YVO$_4$ laser with frequency-shifted feedback," Opt. Commun. **121**(4-6), 137-140 (1995).
34. K. Nakamura, F. Abe, K. Kasahara, T. Hara, M. Sato, and H. Ito, "Spectral characteristics of an all solid-state frequency-shifted feedback laser," IEEE J. Quantum Electron. **33**(1), 103-111 (1997).
35. W. Streifer and J. R. Whinnery, "Analysis of a dye laser tuned by acousto-optic filter," Appl. Phys. Lett. **17**(8), 335-337 (1970).
36. K. Nakamura, T. Miyahara, and H. Ito, "Observation of a highly phase-correlated chirped frequency comb output from a frequency-shifted feedback laser," Appl. Phys. Lett. **72**(21), 2631-2633 (1998).
37. A. Yoshizawa and H. Tsuchida, "Chirped-comb generation in frequency-shifted feedback laser diodes with a large frequency shift," Opt. Commun. **155**(1-3), 51-54 (1999).
38. L. P. Yatsenko, B. W. Shore, and K. Bergmann, "Coherence in the output spectrum of a frequency shifted feedback laser," Opt. Commun. **282**(2), 300-309 (2009).
39. P. A. Bello, "Characterization of randomly time-variant linear channels," IEEE Trans. Commun. Syst. **11**(4), 360-393 (1963).
40. G. J. Spühler, R. Paschotta, R. Fluck, B. Braun, M. Moser, G. Zhang, E. Gini, and U. Keller, "Experimentally confirmed design guidelines for passively Q-switched microchip lasers using semiconductor saturable absorbers," J. Opt. Soc. Am. B **16**(3), 376-388 (1999).
41. E. Desurvire, "Analysis of transient gain saturation and recovery in erbium-doped fiber amplifiers," IEEE Photon. Technol. Lett. **1**(8), 196-199 (1989).
42. O. Pottiez, J. P. Lauterio-Cruz, Y. E. Bracamontes-Rodríguez, H. E. Ibarra-Villalon, J. C. Hernandez-Garcia, M. Bello-Jiménez, and E. A. Kuzin, "Gain-driven spectral-temporal noise-like pulse dynamics in a passively mode-locked fiber laser," Opti. Express **27**(24), 34742-34759 (2019).
43. C. R. Giles, E. Emmanuel, and J. R. Simpson. "Transient gain and cross talk in erbium-doped fiber amplifiers," Opt. Lett. **14**(16), 880-882 (1989).
44. A. K. Srivastava, Y. Sun, J. L. Zyskind, and J. W. Sulhoff, "EDFA transient response to channel loss in WDM transmission system," IEEE Photon. Technol. Lett. **9**(3), 386-388 (1997).
45. G. Luo, J. L. Zyskind, J. A. Nagel, and M. A. Ali, "Experimental and theoretical analysis of relaxation-oscillations and spectral hole burning effects in all-optical gain-clamped EDFA's for WDM networks," J. Lightw. Technol., **16**(4), 527-533 (1998).
46. K. Kuroda and Y. Yoshikuni. "Recovery of population inversion in an erbium-doped fiber amplifier observed by temporally resolving amplified spontaneous emissions," Appl. Opt., **51**(16), 3670-3674 (2012).
47. N. Kanagaraj, L. Djevarhidjian, V. Durán, C. Schnébelin, and H. Guillet de Chatellus, "Optimization of acousto-optic optical frequency combs," Opt. Express **27**(10), 14842-14852 (2019).
48. C. R. Fernández-Pousa and H. Guillet de Chatellus, "Fundamental SNR limits imposed by ASE in frequency shifting loops," J. Lightw. Technol. **40**(20), 6831-6844 (2022).
49. H. Guillet de Chatellus, O. Jacquin, O. Hugon, W. Glastre, E. Lacot, and J. Marklof, "Generation of ultrahigh and tunable repetition rates in CW injection-seeded frequency-shifted feedback lasers," Opt. Express **21**(13), 15065-15074 (2013).
50. H. Guillet de Chatellus, E. Lacot, W. Glastre, O. Jacquin, and O. Hugon, "Theory of Talbot lasers," Phys. Rev. A

88(3), 033828 (2013).

51. J. Goodman, *Statistical Optics* (Wiley, 1985), Chap. 6.